Available online at www.sciencedirect.com
ScienceDirect
Carbon 45 (2007) 2400–2410
CARBON
www.elsevier.com/locate/carbon

Insights on the nanoparticle formation process in counterflow diffusion flames

Seung Hyun Chung, Angela Violi *

Department of Mechanical Engineering, University of Michigan, Ann Arbor, MI 48109-2125, United States

Received 5 May 2007; accepted 6 July 2007
Available online 14 July 2007

Abstract

This paper reports on a new version of the multiscale atomistic model for particle inception (AMPI) code to study the effect of oxidation on nanoparticle structures formed in counter-flow, propene diffusion flames. The code has been expanded with 158 new oxidation reactions and the potential for the Molecular Dynamics module has been expanded to describe systems containing C, H and O. The rate of nanoparticle mass growth is modeled in two different flame configurations to address the influence of combustion environments on the inception process. In the case of high temperature and abundant radicals, the AMPI code successfully predicts the nanoparticle formation. In these conditions, the particle loading is mainly associated with the formation of high-molecular structures through polymerization reactions. In the case of low temperature and high polycyclic aromatic hydrocarbons (PAH) concentrations, the combined mechanism of chemical reactions described by the AMPI code and coagulation of PAH and nanoparticles contribute to particle growth. Structural properties of the particles, such as aspect ratio, oxygen content and H/C ratio are computed in the two configurations.
© 2007 Elsevier Ltd. All rights reserved.

1. Introduction

Soot emissions from a combustion source are much less than the amount actually generated within the system. The difference usually comes from the combustion of soot particles in oxygen-containing regions beyond the soot-formation zone [1]. During the formation of polycyclic aromatic hydrocarbons (PAH) and soot, oxidation reactions often play an important role depending on the flame structure. The effect of oxidation at the molecular level can instigate competing reactions: carbon mass is diverted from further growth, while O and OH can promote formation of soot by building up the radical pool [2]. It is the purpose of this work to get insights on the effects of oxidation environments on nanoparticle growth using computational tools.

Counterflow diffusion flames are very attractive from the standpoint of combustion science, since the flame is spatially much wider than an equivalent premixed flame. Particle formation in counterflow diffusion flames has been extensively investigated for their ability to represent turbulent flames within the laminar flamelet model. For diffusion flames, flow characteristics play an important role in the formation, growth, and oxidation of particles [3,4] and sooting characteristics can be significantly affected by the flame location. When a diffusion flame is located on the fuel side, the gas velocity is directed toward the flame and particles follow the gas-phase streamlines. On the other hand, when the flame is located on the oxidizer side, the gas velocity is directed to the stagnation plane and particles move away from the flame [5]. As a consequence particle growth will be significantly different and this makes the counter-flow diffusion flames very appealing to study the different processes that contribute to the formation of particles.

In this paper we apply a multiscale computational tool, the AMPI code (Atomistic Model for Particle Inception) [6], to study the formation of nanoparticles in different combustion regimes. The specific goal is to address the importance of oxidation reactions on particle growth and the influence of combustion conditions on the structural

* Corresponding author. Fax: +1 734 647 9679.
E-mail address: avioli@umich.edu (A. Violi).

0008-6223/$ - see front matter © 2007 Elsevier Ltd. All rights reserved.
doi:10.1016/j.carbon.2007.07.003

properties of nanoparticles, such as morphology and aspect ratio.

The systems chosen for this computational study are two counterflow diffusion flames experimentally studied by Kang et al. [5]. The availability of experimental data will help to guide and validate the numerical approach.

After a section describing the novel implementations to the computational methodology, two different flame configurations are studied and an analysis of the nanoparticle growth rates, their H/C ratios, and morphologies is reported together with a detailed discussion of the reactions that contribute to particle inception.

2. Methodology

2.1. AMPI algorithm

Particle growth occurs on a time scale that is generally not accessible to fully atomistic models such as molecular dynamics (MD), whereas an atomically resolved Monte Carlo method parameterized by accurate chemical kinetic data is capable of exploring growth over long times and large length scales. The AMPI code proposes a new approach to study the transition from gas-phase to nanoparticles, involving the coupling of kinetic Monte Carlo (KMC) and MD. This coupling provides a key to the multiple time-scales involved in the formation of nanoparticles, spanning pico- or nanoseconds for intramolecular processes that can occur for example on a particle surface to milliseconds for intermolecular reactions [6–9].

As inputs, the AMPI code requires a detailed description of the gas-phase environment that for this work is provided by the OPPDIF code [10] of the CHEMKIN suite of programs, with a chemical model that includes 172 species and 4890 reactions steps up to the C16 mechanism.[1]

After reading a set of inputs, including temperature, species concentrations in the gas-phase and reaction rates, the AMPI code determines the number of sites available for reactions on the growing structure by identifying each atom as a radical, neutral, aliphatic and aromatic site. After that the code checks for steric hindrance, and the reactions available at that time are classified as either accepted or rejected. Once a list of possible reactions is created, along with possible sites and reaction rates, the code randomly selects a reaction based on the reaction probability, and it then modifies the structure of the growing particle according to the selected reaction. Finally the code performs a MD simulation run that allows the newly formed structure to reach thermal equilibrium. The NVT ensemble is used for the simulation and the temperature is set equal to the flame temperature at the location analyzed. The AMPI code alternates between a KMC step and a MD step.

2.2. Flame conditions

Counterflow diffusion flames are frequently located on the oxidizer side when pure hydrocarbon is supplied from the fuel side. Upon appropriate dilution of the fuel and oxidizer streams, however, the flame can be moved to the fuel side [11,12]. A soot formation (SF) flame is obtained when the flame is located on the oxidizer side of a stagnation plane, such that soot particles once formed are convected away from the flame toward the stagnation plane. Thus, soot oxidation is absent. A soot formation/oxidation (SFO) flame occurs when the flame is located on the fuel side such that soot particles are transported toward the high temperature oxidizer side. Due to oxidation, SFO flames demonstrate similar behavior to sooting premixed flames. Fig. 1 reports the schematics for the two configurations.

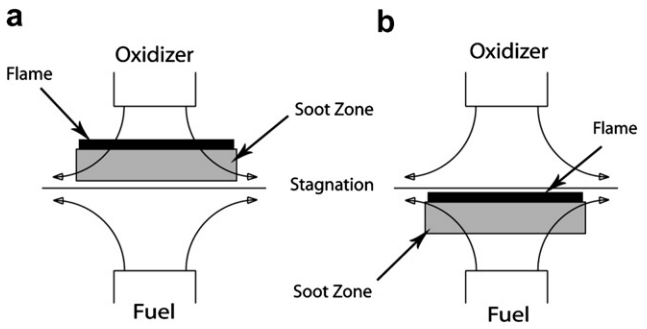


Fig. 1. Schematics of: (a) soot formation (SF) and (b) soot formation–oxidation (SFO) counter flow diffusion flames [5].

For this study we analyzed a SFO and a SF flame of propane. The flame conditions for the SFO flame were $(X_{C_3H_8}, X_{O_2}) = (0.25, 0.7)$ with the fuel flow composed of 25% C_3H_8 in N_2 and the oxidizer stream of 70% O_2 and 30% N_2. The SF flame had $(X_{C_3H_8}, X_{O_2}) = (1.0, 0.3)$. The volume-averaged nozzle exit velocities for the SF and SFO flames were 0.2 m/s for the fuel and oxidizer streams. Both the nozzle exit diameter and the separation distance between the two nozzles were 14.2 mm.

These flames have been experimentally investigated by Kang et al. [5] who employed soot extinction-scattering, PAH fluorescence, and laser Doppler velocimetry measurements to determine the characteristics of the particle zone structures.

3. Results and discussion

3.1. A new version of the AMPI code for C, H, O systems

In order to study the importance of oxidation reactions during the nanoparticle formation process, a new version of the AMPI code (v.2.0) has been implemented and the two major modules, MD and KMC, have been modified accordingly. These modifications include: (i) new oxygen related terms in the AIREBO potential and MD module, (ii) oxygen related reactions in KMC module. With these improvements, the new AMPI code can be used to study complex systems composed of C, H and O atoms.

3.1.1. MD module

To describe the bonded interactions within the Molecular Dynamics module, we used the potential developed by Ni et al. [13], who expanded the second-generation empirical bond order (REBO) potential for hydrocarbons, as parameterized by Brenner and co-workers [14–16], to include covalent C–O, H–O, and O–O interactions. Unlike force field models, this potential allows for chemical bond rupture and bond formation to occur. To increase its utility we then included non-bonded and torsional interactions. For the Lennard–Jones potential, parameters for O–O were taken from the DREIDING force field [17] while C–O and H–O parameters were obtained by the Lorentz–Berthelot combining rules [18] using C–C, H–H and O–O parameters. For the torsional interactions, we considered the following systems: X–C–C–Y combination, X–C–C–O, X–C–O–Y and X–O–O–Y. For the X–C–C–O and X–C–O–Y, the same functional form of AIREBO X–C–C–Y was used and the parameters were obtained from

[1] http://www.chem.polimi.it/CRECKModeling/

ethanol [19] for the X–C–C–O torsional interaction and from methanol [20] for the X–C–O–Y interaction.

For the X–O–O–Y configuration, considering two bonds *IJ* and *KL* connected via a common bond *JK* involving two sp^3 atoms of the oxygen, we used the following functional form [17]:

$$E_{IJKL} = 1/2V_{JK}\{1 - \cos[2(\varphi - 90^\circ)]\}$$

where V_{JK} is the barrier to rotation, φ is the dihedral angle between the *IJK* and *JKL* planes, 90° is the equilibrium angle and 2 is the periodicity. This function is zero at the equilibrium angle and never negative. The rotation barrier (V_{JK}) in the DREIDING force field is 2.0 kcal/mol and this is the same value used in this force field for a dihedral single bond involving two sp^3 carbon atoms. Experimental data on H_2O_2, however, indicate a barrier of 7.33 kcal/mol [21] and, therefore, this last value is used in the AMPI code.

Sometimes stiff LJ potential can prevent bonding reaction if the transition between non-bonded to bonded interaction is not adequate. To assess this point, we looked at the chemistry of gas-phase collisions between phenyl and OH with different kinetic energies and initial conditions. Collisions in the gas phase are simulated by giving OH a translational velocity towards the phenyl. Incident kinetic energies ranged from 0.5 to 10 eV per molecule. In each case, the outcomes of 10 collisions from different initial random molecular orientations were studied. According to the incident energy, phenyl and OH react if OH gets close to the radical on the phenyl while the phenyl and OH repel each other if they are not favorably oriented. When OH is favorable aligned with phenyl and the kinetic energy is less than 6.5 eV, we observed the formation of phenol produced through a new bond between C and O.

3.1.2. KMC module

We implemented the KMC module of the AMPI code with the following reactions to describe the oxidation of nanoparticles:

$$R_i + O \rightarrow R_{i-1} + CO$$
$$R_i\text{–}O + O \rightarrow R_{i-1} + CO_2$$
$$R_i\text{–}H + O \rightarrow R_{i-1} + CO + \frac{1}{2}H_2$$
$$R_i\text{–}H + O/OH \rightarrow R_i + OH/H_2O$$
$$R_i + O/OH \rightarrow R_i\text{–}O/R_i\text{–}OH$$

where R_i–H is an aromatic molecule with *i* pericondensed rings, and R_i is its radical. We also included oxidation reactions occurring on non-aromatic carbon atoms, and a total of 158 new reactions were added to the AMPI code. Some of the key reaction rates are listed in Table 1.

3.2. Soot-formation-oxidation (SFO) flame

Fig. 2 shows the computed results obtained with OPPDIF for the concentrations of propane, oxygen, acetylene, hydroxyl and oxygen radicals together with the temperature profile for the SFO flame ($X_{C_3H_8}, X_{O_2}) = (0.25, 0.7)$. These conditions correspond to a flame location close to the gas-phase stagnation plane. In such case, the soot zone is located on the fuel side and particles are transported toward the particle stagnation plane, that is, toward the higher temperature region, where they finally get oxidized.

The computed temperature values agree well with the measured temperature profile from coherent anti-Stokes Raman spectroscopic measurements reported by Kang et al. [5]. Propane is pyrolyzed to form hydrocarbons such as C_2H_2 that exists in the range $z = 3$–6 mm where z is the distance from the fuel nozzle. In the same figure the computed concentration profile of OH is shown in order to identify the flame location. The particle stagnation plane is located around Point 11 and the luminous zone has been experimentally identified between Points 9 and 12.

To determine the characteristics of the sooting zone, we analyzed several locations in the flame covering 12 Points from the fuel to the oxidizer side. The circles in Fig. 2 show the locations sampled with the AMPI code.

Table 1
Reaction rates in the extended Arrhenius format ($AT^{\beta}e^{-E/RT}$) for some reactions implemented in the KMC module

Reactions	A	β	E_a	Reference
$C_5H_4O + H = CH_2CHCHCH + CO$	2.10E+61	−13.27	40810	[22]
$C_5H_4O + O = C_4H_4 + CO_2$	1.00E+13	0	2000	[22]
$C_5H_5 + O = C_5H_5O$	7.06E+04	1.03	−6960	[23]
$C_5H_5 + OH = C_5H_4OH + H$	2.15E+30	−4.61	25050	[23]
$C_5H_6 + OH = C_5H_5 + H_2O$	3.08E+06	2	0	[23]
$C_6H_5 + O = C_5H_5 + CO$	1.00E+14	0	0	[24]
$C_6H_5 + OH = C_6H_5O + H$	5.00E+13	0	0	[25]
$C_6H_5O + CH_3 = C_6H_5OCH_3$	1.21E+13	0	0	[26]
$C_6H_5O + O = C_5H_5 + CO_2$	1.00E+13	0	0	[22]
$C_6H_5O + O = C_6H_4O_2 + H$	8.50E+13	0	0	[22]
$C_6H_5OH + H = C_6H_6 + OH$	7.10E+12	0	5385	[27]
$C_6H_5OH + O = C_6H_5O + OH$	2.81E+13	0	7352	[28]
$C_6H_5OH + OH = C_6H_5O + H$	5.00E+13	0	0	[25]
$C_6H_5OH + OH = C_6H_5O + H_2O$	2.95E+06	2	−1312	[29]
$C_6H_6 + O = C_6H_5O + H$	2.40E+13	0	4668	[30]
$C_6H_6 + OH = C_6H_5 + H_2O$	2.11E+13	0	4571	[31]
$C_6H_6 + OH = C_6H_5OH + H$	1.32E+13	0	10592	[32]

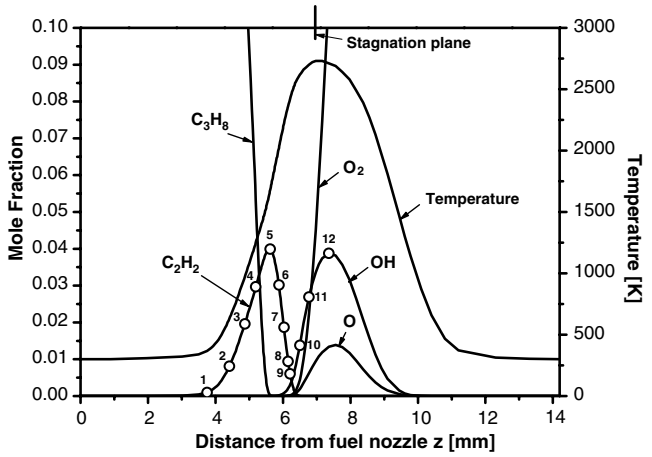


Fig. 2. Numerical results for the temperature profile and C_3H_8, C_2H_2, O_2, OH and O concentrations in the SFO flame. (○) represents the locations sampled by the AMPI code.

Upon inclusion of the gas-phase species concentrations and temperature into the AMPI code, several runs were carried out to study particle formation in these 12 locations. Since the AMPI code follows the growth of a single particle at a specific location in the flame, we generated an ensemble of twenty particles for each location. Fig. 3 shows the number of carbon atoms present on the nanoparticles as a function of time for locations 4 through 7.

At Points 1–3 corresponding to the early formation of acetylene, the particle growth was found to be very slow. For example, at $z = 3.75$ mm (Point 1) the first reaction selected by the KMC module of the AMPI code was hydrogen abstraction and it took 1096 s to proceed, which is very slow when compared with the flame velocity at that point (11.23 cm/s). Towards the peak of acetylene the growth rate increased dramatically.

At $z = 5.19$ mm (Point 4) particle growth occurs on the order of 10^{-3} s as shown in Fig. 3 and in the same location the gas velocity is ~10 cm/s. If we assume that particle's velocity is similar to the gas velocity, the particle formed in Point 4 would proceed $O(10^{-3}\ s) * O(10\ cm/s) = O(0.1\ mm)$ and with the distance between locations 4 and 5 being around 0.43 mm, the particle might be convected away to Point 5 before it significantly increases in size. The nanoparticle growth rate dramatically changes between locations 4 and 5. At location 5, particle growth took $O(10^{-4}\ s)$ and since the gas velocity at this point is similar to the one in location 4, particles move O(0.01 mm). According to these results, we can conclude that the particle inception becomes significant in this SFO flame between locations 4 and 5 where the concentration of acetylene reaches its peak. The computational results are in very good agreement with the experimental values reported by Kang et al. [5], where the measured rise in the PAH signal (Q_f) and scattering signal (Q_{vv}) profiles were shown to begin at 4 mm and 5 mm, respectively. This indicates that the particle inception process is well described by the AMPI code in this environment. At

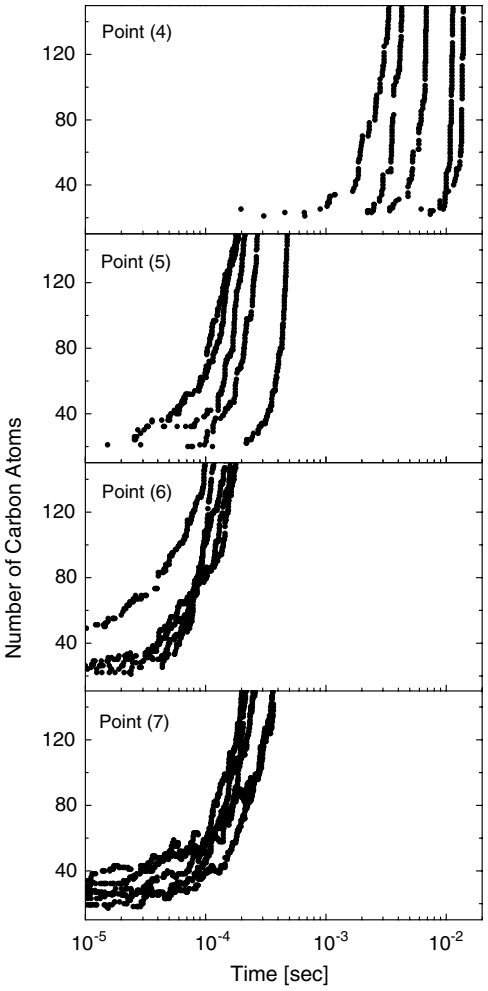


Fig. 3. Number of carbon atoms on the particle as a function of time for $z = 5.19$ mm (Point 4), $z = 5.62$ mm (Point 5), $z = 5.88$ mm (Point 6) and $z = 6.03$ mm (Point 7).

$z = 5.62$ mm (Point 5), $z = 5.88$ mm (Point 6) and $z = 6.03$ mm (Point 7), the computed growth rates are similar because of two counterbalancing effects. As we move toward the stagnation plane, the temperature increases going from 1700 K at Point 5 to 2200 K at Point 7, and the concentrations of hydrocarbons, including acetylene, decreases. Fig. 4 reports examples of particle configurations obtained at Points 5, 6 and 7.

Table 2 lists the main reactions occurring at Points 5, 6 and 7. Ring closure reactions, in which nascent rings are formed through dehydrogenation mechanisms [33], acetylene addition and hydrogen eliminations and additions are the most frequent reactions. The importance of C_2H_2 in early inception zone is also in agreement with the experimental data by Kang et al. which shows the coincidence of the maximum values of PAH fluorescence, soot particle number density, at the point of the onset of the scattering signal indicates that the particle inception occurs from PAH through C_2H_2.

Ethylene addition to radicals on the growing seed plays a significant role at Point 4, but this contribution diminishes faster than the contribution of acetylene as we move

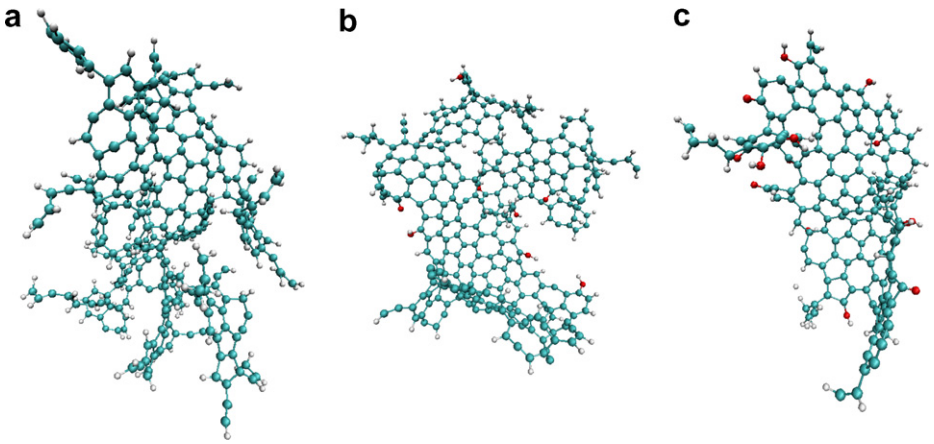


Fig. 4. Carbonaceous nanoparticles produced by the AMPI code at Points 5 (a), 6 (b), and 7 (c). Carbon atoms are shown in blue, hydrogen atoms are silver and oxygen atoms are red. (For interpretation of the references to colour in this figure legend, the reader is referred to the web version of this article.)

Table 2
Principal reactions occurring in the particle inception region of the SFO flame

Reactions	% at Point 5	% at Point 6	% at Point 7
Cyclodehydrogenation	18.2	15.1	8.0
Abstraction reactions			
Hydrogen abstraction by H radical	13.8	14.5	14.2
Hydrogen abstraction by CH_3 radical	9.3	3.9	0.8
Hydrogen abstraction by OH radical	2.3	7.5	11.1
Addition reactions			
C_2H_2	31.7	23.2	10.8
C_2H_4	6.9	1.1	0.1
C_4H_2	0.9	0.5	0.2
CH_3	2.2	0.6	0.2
H	12.4	26.3	35.7

towards the stagnation plane, since the C_2H_4 concentration starts decreasing at 5.3 mm while acetylene peaks at 5.6 mm (Point 5).

In the region from $z = 5.6$ to 6 mm (Points 5–7) hydrogen addition to radical sites on the particle is significant and this causes a reduction of the number of reactive sites on the growing seed. At Point 5 ($z = 5.62$ mm), hydrogen abstraction by CH_3 also significantly contribute to the particle growth. At $z = 5.88$ mm corresponding to Point 6, hydrogen abstraction by OH becomes important.

3.2.1. H/C ratio

H/C ratios of the particles generated at locations 5, 6 and 7 are reported in Fig. 5 as function of time. We carried out the simulations until particles of similar sizes were produced by the AMPI code. Low values of the H/C ratios at $z = 5.88$ mm (Point 6) and 6.03 mm (Point 7) are indicative of more aromatic structures as compared to higher values of H/C ratios obtained at $z = 5.62$ mm, location 5. This is due to the significant concentration of hydrocarbons that can react with the particle and to the cyclodehydrogenation reactions in which hydrogen atoms are lost, and a new ring is created by the formation of a new transannular C–C bond [33,34]. At Point 5 the low temperature ($T \sim 1680$ K) causes a low rate of the cyclodehydrogenation reactions.

3.2.2. Aspect ratio

Ellipticity parameters are often used to characterize particle morphology. To this end, the aspect ratio AR, defined as AR = a/b where a is a major axis and b is a minor axes of the particle is computed to get insights on the shape of the particles formed in flame. Fig. 6 shows the aspect ratios of particles at locations 5, 6 and 7 in the flame. The AR of a circle is one and of an ellipse with the ratio of axes 2:1 is equal to two.

The results reported at Point 7 are due to particle fragmentation. Once the particle divides in smaller systems, the AMPI code follows the growth of the largest fragment.

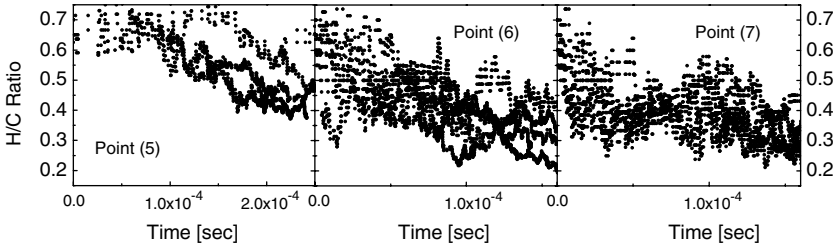


Fig. 5. H/C ratios of nanoparticles at Points 5, 6 and 7 as a function of time.

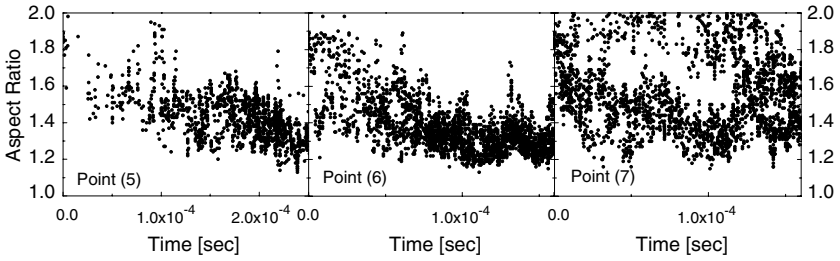


Fig. 6. Aspect ratios of nanoparticles at Points 5, 6 and 7 as a function of time.

3.2.3. Oxidation

At $z = 6.15$ mm (Point 8 in Fig. 2) oxidation reactions start to play an important role and we did not observe particle growth beyond this location. To study the effect of oxidation, we used a particle produced at Point 7 – $C_{90}H_{44}O_5$ as initial seed for the analyses at Points 8 through 12. The reason for this approximation was to determine the effects of O and OH radicals, despite the fact that likely a particle formed at Point 7 would undergo further chemical reactions, coagulation growth and other mechanisms before it reaches the oxidation region.

Fig. 7 shows the number of carbon atoms present on the growing species as a function of time at locations 8–12. The curves are representative of different runs. The decrease at long time is indicative of the breakdown of the particles into small fragments. At $z = 6.15$ mm (Point 8), some particles are reduced in size and others undergo addition from the gas phase. Around $z = 6.21$ mm, location 9, the mole fractions of OH and C_2H_2 become almost equal and the burnout is significant. The contributions of OH and O to the particle growth are twofold: they remove carbon from the nanoparticle producing CO and CO_2 and they react with radicals on the particle, preventing further addition of hydrocarbons.

From Point 8 toward the oxidizer stream, an increasing concentration of OH radicals oxidizes the particles causing a decrease of the particle sizes. This result agrees well with the experimental data showing after $z = 6$ mm a decrease in the particle size and volume fraction. Although a decrease of PAH is mitigated by the formation of PAH from the oxidation of particles, the net amount of PAH gradually decreases because of oxidation by radicals such as OH. This counterflow flame located near the stagnation plane can be classified as a soot formation-oxidation flame as the particle mechanism is dominated by oxidation.

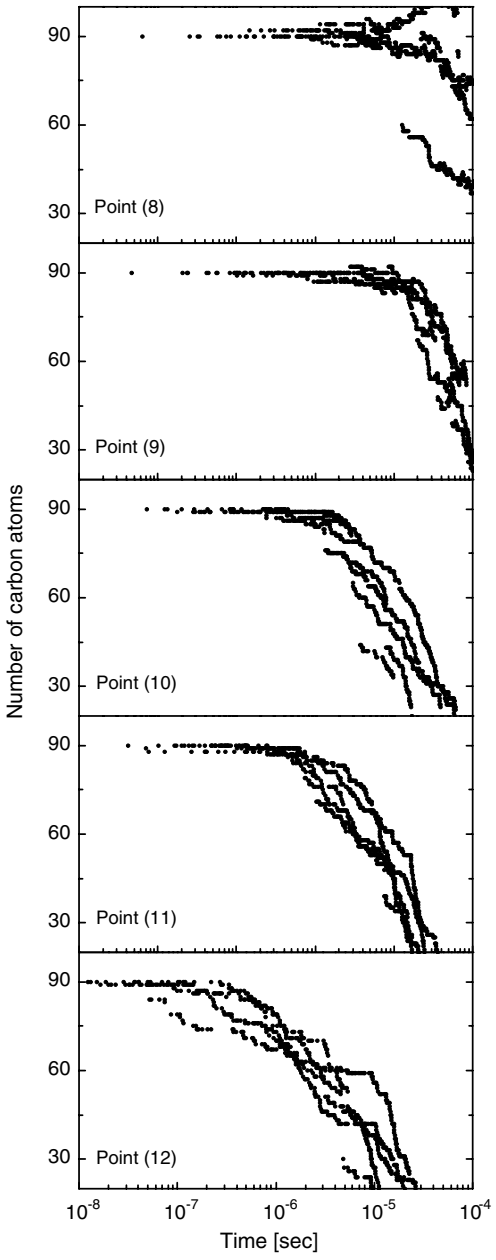


Fig. 7. Number of carbon atoms on the particle as a function of time for $z = 6.15$ mm (Point 8), $z = 6.21$ mm (Point 9), $z = 6.50$ mm (Point 10), $z = 6.77$ mm (Point 11) and $z = 7.36$ mm (Point 12).

3.3. Soot-formation (SF) flame

Fig. 8 illustrates the computed profiles of temperature and species concentrations for the soot-formation (SF) flame $(X_{C_3H_8}, X_{O_2}) = (1.0, 0.3)$. In this case, the soot zone is located on the oxidizer side in the region of 5 mm $< z <$ 7 mm, next to the flame zone of 7.5 mm $< z <$ 8.5 mm and particles are transported away from the flame toward the fuel side. In a manner similar to the previous flame, we analyzed 10 locations in the flame to study particle growth. The locations are reported in Fig. 8.

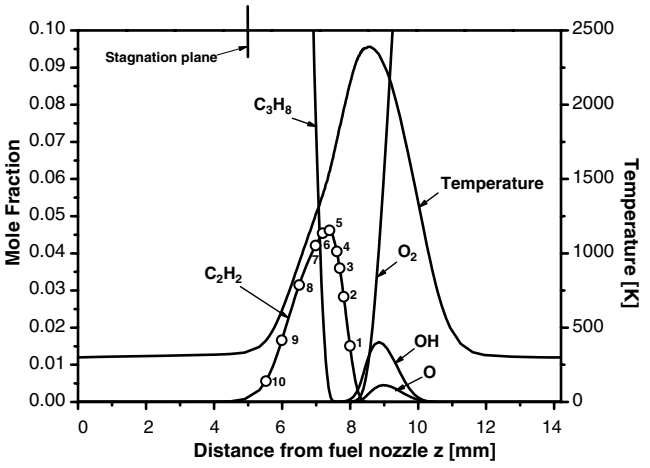


Fig. 8. Numerical results for the temperature profile and C_3H_8, C_2H_2, O_2, OH and O concentrations in the SF flame. (○) represents the locations sampled by the AMPI code.

Fig. 9 shows the change in number of carbon atoms on the growing particle as function of time for Points 3 through 7. No significant particle growth was computed at Points 1 and 2 ($z = 8.0$ mm and $z = 7.8$ mm, respectively). At Point 3, $z = 7.7$ mm, particle growth suddenly becomes significant. The computational results are in agreement with the experimental measurements by Kang et al. [5] showing that the soot inception is located around $z \sim 7$ mm, having almost the same temperature as in the case of the SFO flame (Point 5). Nanoparticles are formed in the region between the flame front and the maximum aromatic concentration since the presence of H-atoms initiates the growth process. The fastest growth rate was computed at $z = 7.7$ mm (Point 3) and $z = 7.6$ mm (Point 4) and no significant growth was obtained after Point 7 due to the low temperature and rapid decrease of hydrocarbon concentrations.

Fig. 10 shows examples of particle configurations formed at various locations in the flame. Differently from the SFO flame, at Point 3, where the particle inception begins, we observed oxygen atoms on the particle. We identified a maximum concentration of 15% of oxygen atoms on the particles. The number of oxygen atoms on the particle decreases moving further from the flame front.

Fig. 11 shows the change in H/C ratio for the particles produced at Points 3–5 together with the change in the aspect ratio. The values and trends are very similar to the ones reported for the SFO flame.

Table 3 reports the major reactions occurring at Points 3, 4, 5, 6 and 7. Acetylene additions still play an important role and PAH contribution to particle growth is not significant in this region.

Going from Point 3 to Point 7, the contribution of hydrogen abstraction by hydrogen and OH radicals to particle growth decreases while hydrogen abstractions by hydrocarbon radicals becomes more frequent. Hwang et al. suggested that in the particle growth region, hydrocarbon radicals are likely responsible for the growth by

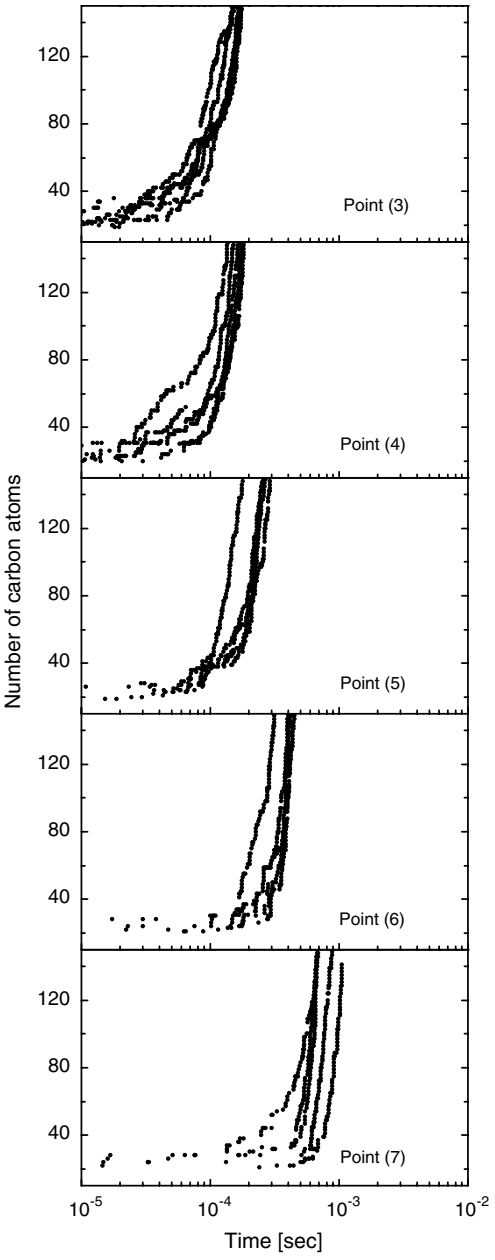


Fig. 9. Number of carbon atoms on the growing particle as function of time in the SF flame at $z = 7.7$ mm (Point 3), $z = 7.6$ mm (Point 4), $z = 7.4$ mm (Point 5), $z = 7.2$ mm (Point 6) and $z = 7.0$ mm (Point 7).

abstracting hydrogen and producing radical sites on the surface of particles [11,12]. Our results reported in Fig. 9, however, show that the particle growth rate significantly drops after Point 4 even though the above mentioned reactions were included. To assess the importance of hydrogen abstractions by hydrocarbons, we conducted a sensitivity analysis by switching off these reactions in the AMPI code. Fig. 12 reports the change of number of carbon atoms with time without hydrogen abstraction by hydrocarbon radicals for Points 3–7. When comparing Figs. 9 and 11, we notice that hydrogen abstraction reactions by hydrocarbon radicals contribute to the particle growth for Points 5 through 7 but their contribution was not significant enough

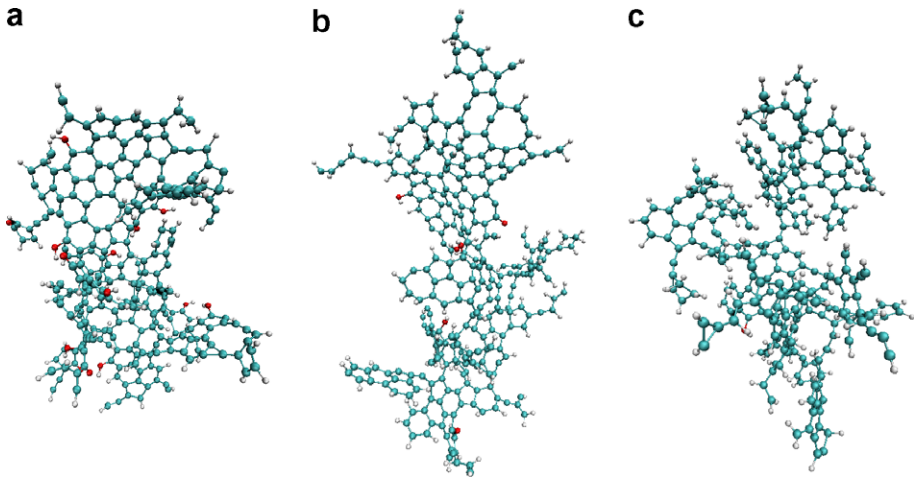


Fig. 10. Carbonaceous nanoparticles produced by AMPI code at Points 3 (a), 4 (b) and 5 (c). Carbon atoms are shown in blue, hydrogen atoms are silver and oxygen atoms are red. (For interpretation of the references to colour in this figure legend, the reader is referred to the web version of this article.)

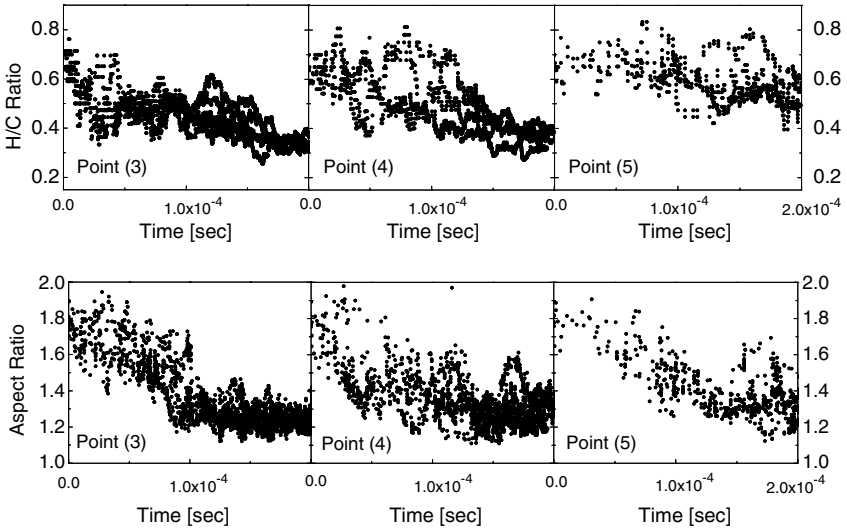


Fig. 11. H/C ratio and Aspect Ratio of nanoparticles produced at Point 3 through 5 in the SF flame.

Table 3
Major reactions in the soot inception region of SF flame

Reaction	% at Point 3	% at Point 4	% at Point 5	% at Point 6	% at Point 7
Cyclodehydrogenation reactions	10.6	14.0	16.7	16.0	14.8
Abstraction reactions					
Hydrogen abstraction by H radical	13.8	12.5	10.2	9.7	7.0
Hydrogen abstraction by CH_3 radical	2.3	5.2	8.0	12.0	16.4
Hydrogen abstraction by OH radical	10.2	7.2	3.8	1.5	0.8
Addition reactions					
C_2H_2	20.3	29.9	36.4	34.7	33.1
C_2H_4	0.3	2.2	6.7	10.6	14.4
C_4H_2	0.4	0.7	0.4	0.8	0.9
CH_3	0.4	1.0	2.2	3.2	3.1
H	28.7	21.2	11.7	9.5	7.4
PAH	0.0	0.0	0.2	0.6	1.1

to change the overall rates. This is mainly due to the temperature drop in this region. In summary, hydrogen abstractions by hydrocarbon radicals are not a major factor to boost particle growth in low temperature region.

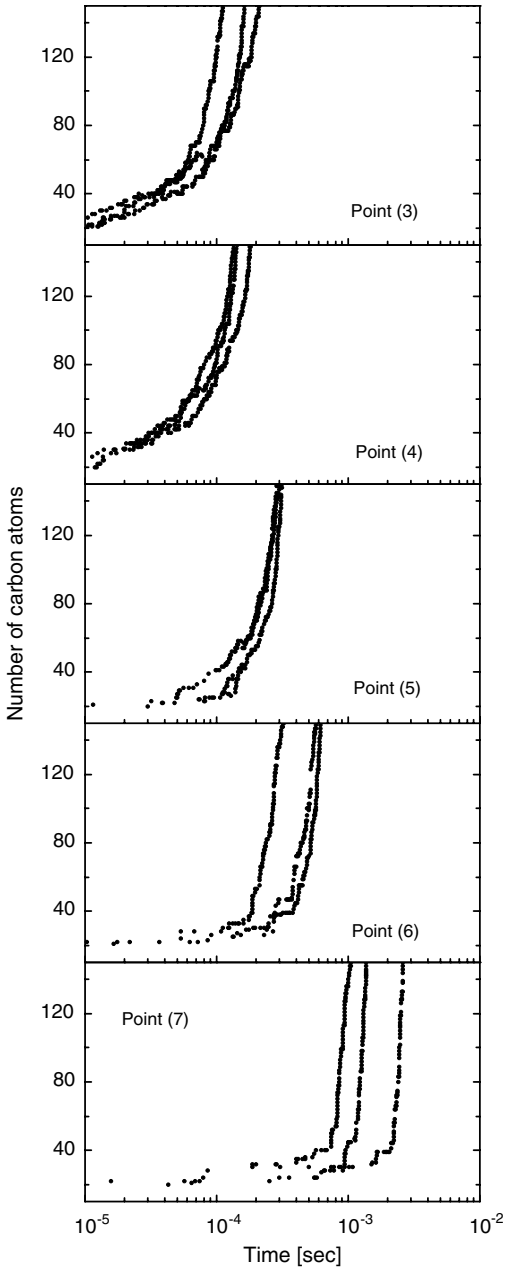


Fig. 12. SF flame without hydrogen abstraction reaction by hydrocarbon radicals. Number of carbon in a particle as a function of time for $z = 7.7$ mm (Point 3), $z = 7.6$ mm (Point 4), $z = 7.4$ mm (Point 5), $z = 7.2$ mm (Point 6) and $z = 7.0$ mm (Point 7).

When comparing the computational results reported in Fig. 9 with the experimental data by Kang et al., we can conclude that particle inception based solely on the chemical growth via C_2H_2 and PAH is not adequate to describe the particle growth in this flame, where the temperature is relatively low (see Fig. 8), while the PAH concentrations are much higher than in the SFO flames. As the stagnation plane is approached ($z = 5$ mm) with the decrease in temperature, the inception rate due to the chemical growth of PAH is decreased while PAH concentrations are continuously increased until the gas stagnation plane is reached. Hence, soot inception via PAH agglomeration instead of PAH growth through the H-abstraction–C_2H_2 addition (HACA) reactions can be a viable particle formation process under these conditions [12,35–37].

Since the inception process based only on chemical interactions does not justify the growth rate identified in flames, we considered the physical process due to coagulation of PAH on nanoparticles. The steady-state rate of collision for a single particle on a bath of PAH for a simple Brownian coagulation is [38]:

$$J_{\mathrm{col}} = K(R_{\mathrm{PAH}}, R_{\mathrm{Nanoparticle}}, D) \cdot N_{\mathrm{PAH}}$$

where the R_{PAH} and $R_{\mathrm{Nanoparticle}}$ are the radii of PAH and nanoparticle, respectively, D is the diffusion coefficient and N_{PAH} is the number concentration of PAH. The number density of PAH is proportional to the collision rate for this simplified model. To clarify the importance of this process in the inception regions of the flames, Fig. 13 reports the total concentration of aromatic species in the SF and SFO flames. Aromatic species concentration is defined as the sum of aromatic species obtained from the Chemkin results and include as main species C_5H_5, C_5H_6, C_6H_5, C_6H_6, C_6H_8, C_6H_{10}, $C_6H_5C_2H$, $C_6H_5C_2H_2$, $C_6H_5C_2H_3$, indenyl, naphthalene, naphthyl, acenapthalene and acenapthyl. The concentration of aromatic species in the particle inception region of the SF flame (grey area) is almost twice that of the inception zone of the SFO flame (2.8×10^{-8} vs. 1.5×10^{-8}). As a consequence, PAH coagulation is expected to be more significant in the SF flame than in the SFO flame.

In summary, particle inception can be considered as the result of a chemical growth and a physical process involving PAH and nanoparticles coagulation. The contribution of these pathways to the particle inception rate varies according to the combustion conditions. In situations where the temperature is relatively high and radicals are abundant (SFO flame) the inception rate is well described

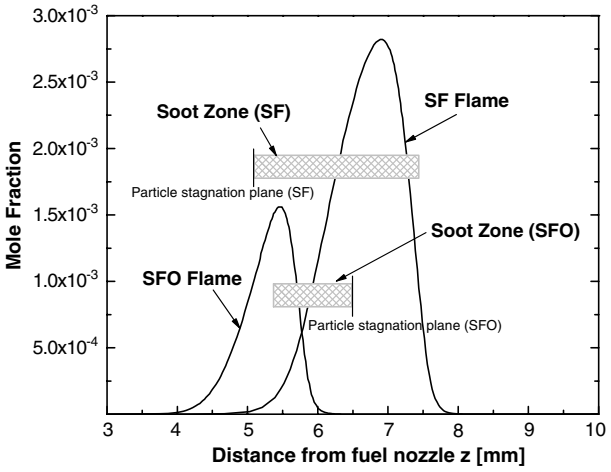


Fig. 13. Sum of aromatic species concentrations for SF and SFO flames. Soot zones of both flames are approximately indicated as crossed gray boxes.

by the AMPI code (chemical growth). At relatively lower temperature and significant PAH concentration (later part of SF flame), particle growth is mainly due to physical coagulation of PAH and nanoparticles rather than chemical growth which can be described by the AMPI code.

Future study will include the analysis of the coagulation processes between particle and PAH and particle–particle about how much they can contribute to the growth of particle to compensate the gap between actual particle growth rate and particle growth via chemically specific way.

4. Conclusions

In this paper we investigated the particle formation characteristics of counter flow diffusion flames using a new version of the multiscale AMPI code that we implemented to describe oxygen-containing systems. One hundred and fifty-eight new oxidation reactions were added to the code and the potential for the Molecular Dynamics module was expanded to describe systems containing C, H and O.

Soot formation characteristics in counterflow diffusion flames can be categorized into soot formation/oxidation flame (SFO) and soot formation flame (SF), based on the relative position between the flame and the particle stagnation plane. In the SFO flame the soot zone is located on the fuel side of both the particle stagnation and the maximum temperature location. The AMPI code was used to describe the inception process in both configurations and structural properties of the nanoparticles, including H/C ratio and aspect ratio, were computed.

The AMPI code that describes the particle inception via chemical reactions, is able to reproduce very well the experimental trends observed by Kang et al. [5] for the SFO flame. We determined the particle formation zone computing the nanoparticle growth rates at 12 locations in the flame. The growth rate was significant in the region where C_2H_2 reached its peak and the main reaction sequence contributing to the growth was the HACA mechanism.

For these flames, the inception region is characterized by high temperature (~2200 K) and relatively high concentration of H and PAH. Particles, once generated are transported towards the higher temperature region and eventually they pass through an O and OH abundant zone to be oxidized. Oxidation regions were also well predicted by the AMPI code. Oxidation reactions competed with surface growth by diverting carbon atoms (e.g., $R_i + O = R_{i-1} + CO$ and $R_i\text{–}H + O = R_{i-1} + CO + 1/2H_2$) and terminating radicals present on the growing structure ($R_i\text{–}H + O/OH = R_i + OH/H_2O$).

For the SF flame, we analyzed ten points using the AMPI code. In this flame, the soot zone is on the oxidizer side of the stagnation plane and the flow field is directed towards the fuel stream in the region between the flame and the particle stagnation plane. Particles, generated on the fuel side of the flame, are transported away from the flame. As a result, they can not pass through the flame and they are not exposed to oxidizing species, such as OH and O_2.

At the very beginning of the particle inception zone, the kinetic growth mechanism embedded in the AMPI code was able to describe particle formation due to the high concentration of C_2H_2 and high temperature (~1900 K).

As soon as the temperature decreases (~1300 K), the chemical growth is not enough to explain the inception rate experimentally identified in this region by Kang et al. To explain this evidence, a different process involving agglomeration of nanoparticles and PAH coagulation on nanoparticles needs to be invoked to be responsible for the soot volume fractions in the low-temperature region of this flame.

In conclusions, particle inception can be considered as the results of two contributions: a chemical growth and a physical process involving agglomeration and coagulation of PAH and nanoparticles. The combustion environment (temperature, H and PAH concentrations) dictates the relative contribution of these processes to the inception growth rate.

Acknowledgements

This research is funded by the National Science Foundation Grant CTS 0553764 and by the Nanoscale Interdisciplinary Research Team Grant (EEC-0304433). The authors thank Prof. S.B. Sinnott for the CHO REBO potential and Dr. D. Wang for the preliminary implementation of oxygen into the MD module.

References

[1] Haynes BS, Wagner HG. Soot formation. Prog Energ Combust Sci 1981;7(4):229–73.
[2] Frenklach M. Reaction mechanism of soot formation in flames. Phys Chem Chem Phys 2002;4(11):2028–37.
[3] Du J, Axelbaum RL. The effect of flame structure on soot-particle inception in-diffusion flames. Combust Flame 1995;100(3):367–75.
[4] Violi A, D'Anna A, D'Alessio A, Sarofim AF. Modeling aerosol formation in opposed-flow diffusion flames. Chemosphere 2003;51(10):1047–54.
[5] Kang KT, Hwang JY, Chung SH, Lee W. Soot zone structure and sooting limit in diffusion flames: comparison of counterflow and co-flow flames. Combust Flame 1997;109(1–2):266–81.
[6] Violi A. Modeling of soot particle inception in aromatic and aliphatic premixed flames. Combust Flame 2004;139(4):279–87.
[7] Violi A, Sarofim AF, Voth GA. Kinetic Monte Carlo molecular dynamics approach to model soot inception. Combust Sci Technol 2004;176(5–6):991–1005.
[8] Violi A, Venkatnathan A. Combustion-generated nanoparticles produced in a benzene flame: a multiscale approach. J Chem Phys 2006;125(5).
[9] Violi A, Voth GA, Sarofim AF. The relative roles of acetylene and aromatic precursors during soot particle inception. Proc Combust Inst 2005;30:1343–51.
[10] Lutz AE, Kee RJ, Grcar JF, Rupley FM. OPPDIF: a fortran program for computing opposed-flow diffusion flames; 1996.
[11] Hwang JY, Lee W, Kang HG, Chung SH. Synergistic effect of ethylene–propane mixture on soot formation in laminar diffusion flames. Combust Flame 1998;114(3–4):370–80.
[12] Hwang JY, Chung SH. Growth of soot particles in counterflow diffusion flames of ethylene. Combust Flame 2001;125(1–2):752–62.

[13] Ni B, Lee KH, Sinnott SB. A reactive empirical bond order (REBO) potential for hydrocarbon-oxygen interactions. J Phys Condens Matter 2004;16(41):7261–75.
[14] Brenner DW, Shenderova OA, Harrison JA, Stuart SJ, Ni B, Sinnott SB. A second-generation reactive empirical bond order (REBO) potential energy expression for hydrocarbons. J Phys Condens Matter 2002;14(4):783–802.
[15] Brenner DW. The art and science of an analytic potential. Physica Status Solidi B-Basic Res 2000;217(1):23–40.
[16] Brenner DW. Empirical potential for hydrocarbons for use in simulating the chemical vapor-deposition of diamond films. Phys Rev B 1990;42(15):9458–71.
[17] Mayo SL, Olafson BD, Goddard WA. Dreiding – a generic force-field for molecular simulations. J Phys Chem 1990;94(26):8897–909.
[18] Hudson GH, McCoubrey JC. Intermolecular Forces between Unlike Molecules – a More Complete Form of the Combing Rules. Trans Faraday Soc 1960;56(6):761–6.
[19] Senent ML, Smeyers YG, Dominguez-Gomez R, Villa M. Ab initio determination of the far infrared spectra of some isotopic varieties of ethanol. J Chem Phys 2000;112(13):5809–19.
[20] Xu LH, Lees RM, Hougen JT. On the physical interpretation of torsion-rotation parameters in methanol and acetaldehyde: comparison of global fit and ab initio results. J Chem Phys 1999;110(8):3835–41.
[21] Flaud JM, Camypeyret C, Johns JWC, Carli B. The far infrared-spectrum of H_2O_2 – 1st observation of the staggering of the levels and determination of the cis barrier. J Chem Phys 1989;91(3):1504–10.
[22] Maria U. Alzueta PGKD-J. Experimental and kinetic modeling study of the oxidation of benzene. Int J Chem Kinet 2000;32(8):498–522.
[23] Zhong X, Bozzelli JW. Thermochemical and kinetic analysis of the H, OH, HO_2, O, and O_2 association reactions with cyclopentadienyl radical. J Phys Chem A 1998;102(20):3537–55.
[24] Frank P, Herzler J, Just T, Wahl C. High temperature reaction of phenyl oxidation. In: Twenty-fifth symposium (international) on combustion. Pittsburgh: The Combustion Institute; 1994. p. 833.
[25] Miller JA, Melius CF. Kinetic and thermodynamic issues in the formation of aromatic compounds in flames of aliphatic fuels. Combust Flame 1992;91(1):21–39.
[26] Tsang W, Hampson RF. Chemical kinetic data base for combustion chemistry. Part I. Methane and related compounds. J Phys Chem Ref Data 1986;15(3):1087–279.
[27] Manion JA, Louw R. Rates, products, and mechanisms in the gas-phase hydrogenolysis of phenol between 922 and 1175 K. J Phys Chem 1989;93(9):3563–74.
[28] Emdee JL, Brezinsky K, Glassman I. A kinetic model for the oxidation of toluene near 1200 K. J Phys Chem 1992;96(5):2151–61.
[29] Knispel R, Koch R, Siese M, Zetzsch C. Ber Bunsenges Phys Chem 1990;94:1375.
[30] Ko T, Flaherty WF, Fontijn A. Flow-tube kinetics study of the reaction between ground-state hydrogen atoms and nitromethane. J Phys Chem 1991;95(18):6967–70.
[31] Madronich S, Felder W. Kinetics and mechanism of the reaction of hydroxyl with benzene. J Phys Chem 1985;89(16):3556–61.
[32] Baulch DL, Cobos CJ, Cox RA, Esser C, Frank P, Th J, et al. Evaluated kinetic data for combustion modelling. J Phys Chem Ref Data 1992;21(3):411–734.
[33] Violi A. Cyclodehydrogenation reactions to cyclopentafused polycyclic aromatic hydrocarbons. J Phys Chem A 2005;109(34):7781–7.
[34] Violi A, Truong TN, Sarofim AF. Kinetics of hydrogen abstraction reactions from polycyclic aromatic hydrocarbons by H atoms. J Phys Chem A 2004;108(22):4846–52.
[35] Frenklach M, Wang H. In: Twenty-third symposium (international) on combustion. Pittsburgh: The Combustion Institute; 1990. p. 1559–66.
[36] Harris SJ, Weiner AM. In: Twenty-second symposium (international) on combustion. Pittsburgh: The Combustion Institute; 1988. p. 333–42.
[37] Macadam S, Beer JM, Sarofim AF, Hoffmann AB. Soot surface growth by polycyclic aromatic hydrocarbon and acetylene addition. In: Anon, editor. Symposium (international) on combustion. Napoli, Italy: Combustion Institute; 1996. p. 2295–302.
[38] Seinfeld JH, Pandis SN. Atmospheric chemistry and physics: from air pollution to climate change. New York (NY): Wiley & Sons, Inc; 1997. p. 656–9.